Research Article

Ni$_{1-x}$Pt$_x$ ($x = 0$–0.08) Films as the Photocathode of Dye-Sensitized Solar Cells with High Efficiency

Shengjie Peng, Jifu Shi, Juan Pei, Yanliang Liang, Fangyi Cheng, Jing Liang, and Jun Chen (✉)

Institute of New Energy Material Chemistry, Key Laboratory of Energy Material Chemistry, and Engineering Research Center of High-Energy Storage and Conversion, Ministry of Education, Nankai University, Tianjin 300071, China

ABSTRACT

Films of Ni$_{1-x}$Pt$_x$ ($x = 0$, 0.02, 0.04, 0.06, and 0.08) have been prepared on fluorine-doped tin oxide-coated (FTO) glass substrates by a chemical plating method and used as the photocathode for dye-sensitized solar cells (DSCs). The Ni$_{0.94}$Pt$_{0.06}$ film consisted of nanoparticles with a size of 4–6 nm and a Pt loading of 5.13 μg/cm^2. The Ni$_{0.94}$Pt$_{0.06}$ photocathode exhibited high catalytic performance toward triiodide reduction, high light reflectance, and low charge-transfer resistance. The DSC assembled with the Ni$_{0.94}$Pt$_{0.06}$ photocathode gave a short-circuit photocurrent density (J_{sc}) of 16.79 mA/cm^2, an open-circuit photovoltage (V_{oc}) of 736 mV, and a fill factor (FF) of 66.4%, corresponding to an overall conversion efficiency of 8.21% under standard AM 1.5 irradiation (100 mW/cm^2), which is higher than that for the DSC with a pure Pt photocathode obtained by conventional thermal decomposition. Furthermore, the DSC based on the Ni$_{0.94}$Pt$_{0.06}$ photocathode showed good stability. The results indicate that Ni$_{0.94}$Pt$_{0.06}$ films are promising low-cost and high-performance photocathodes for use in DSCs.

KEYWORDS

Introduction

With the consumption of the earth's fossil fuels, developing new advanced materials for energy storage and conversion with high efficiency is driving more and more research interest [1–4]. In recent years, dye-sensitized solar cells (DSCs) based on TiO$_2$ films have received much attention due to their low-cost fabrication and relatively high conversion efficiency [5]. The photocathode of DSCs, which enables the transfer of electrons from the external circuit back to the redox electrolyte and catalyzes the reversible conversion of the iodide/triiodide (I$^-$/I$_3^-$) redox couple, usually utilizes platinum-based films [6, 7]. Among various methods for the preparation of Pt films, thermal decomposition of H$_2$PtCl$_6$ solution is the most common approach. The as-obtained Pt film has a low Pt loading and shows higher catalytic performance than Pt films obtained by other methods such as sputtering [8], electrochemical deposition [9], and dip coating [10]. More recently, bilayer films such as Pt/Ti [11], Pt/NiO [12], and Pt/NiP [13] as the photocathode of DSCs have been prepared through vacuum sputtering or thermal decomposition at

relatively high temperatures of about 400 °C. These methods normally need complex facilities or high-temperature operation and thus are not suitable for large-scale production. Therefore, developing a facile method to fabricate photocathodes with high conversion efficiency is a critical step in the development of commercial DSCs.

Herein, we report the fabrication of $Ni_{1-x}Pt_x$ films, composed of alloy nanoparticles with sizes of 4–6 nm, on fluorine-doped tin oxide-coated (FTO) glass substrates by a facile chemical method at room temperature, which is economical in both its consumption of materials and energy requirements. The catalytic performance toward triiodide redox reactions of the as-prepared $Ni_{0.94}Pt_{0.06}$ film as a photocathode in a DSC cell is investigated in detail.

1. Experimental

1.1 Fabrication of $Ni_{1-x}Pt_x$ samples

FTO glass with square resistance of 20 Ω was successively cleaned ultrasonically in acetone, distilled water and ethanol baths for 30 min each. The fabrication of $Ni_{1-x}Pt_x$ films involves three steps: the pretreatment of the substrates including sensitization and activation processes, the coating of Ni films by chemical plating, and the formation of $Ni_{1-x}Pt_x$ films by the reaction of Ni films with H_2PtCl_6 solution. The preparation of $Ni_{1-x}Pt_x$ films is schematically shown in Fig. 1. Detailed procedures are as follows.

First, the FTO glass substrate was dipped in a 0.01 mol/L $SnCl_2$ solution for 15 min to afford adsorbed $SnCl_2$. Second, the substrate was placed in a 0.03 mol/L $PdCl_2$ solution for 10 min. The $PdCl_2$ reacted with $SnCl_2$ on the glass substrate to afford Pd nanoparticles, which act as a catalyst in the subsequent formation of the Ni film [14].

Third, the substrate coated with Pd was vertically immersed in an aqueous solution containing 0.058 mol/L of sodium potassium tartrate hexahydrate ($NaKC_4H_4O_6\cdot6H_2O$) and 0.017 mol/L of $NiSO_4\cdot6H_2O$ at room temperature. Then, a fresh 0.01 mol/L solution of $NaBH_4$ in aqueous NaOH as the reductant was added slowly to the above solution. After 1 h, the conductive surface of the FTO glass substrate changed from colourless to black, indicating the formation of a Ni film on the bare FTO glass [15]. However, there was no visible solid on the non-conductive surface of the FTO glass substrate (see Fig. S-1 in the Electronic Supplementary Material (ESM)). This may be due to the different roughness of the conductive side and the non-conductive side of the substrate; it is known that the FTO nanoparticles on the conductive surface can facilitate the growth of Ni films [16] The Ni film was washed with water and ethanol and dried at 100 °C for 1 h in vacuum to enhance its adhesion to the substrate. Finally, the formation of $Ni_{1-x}Pt_x$ films was carried out by the redox reaction of the Ni films with a 1 mmol/L aqueous solution of H_2PtCl_6 for different times.

The $Ni_{1-x}Pt_x$ thin films obtained with reaction times of 0 s, 15 s, 30 s, 45 s, and 60 s are denoted as (I), (II), (III), (IV), and (V), respectively. For comparison, a Pt film denoted as (VI) was prepared by spin-coating FTO conductive glass with a 10 mmol/L solution of H_2PtCl_6 in isopropanol followed by thermal decomposition of the H_2PtCl_6 at 380 °C for 30 min. Photos of the FTO conductive glass and samples (I), (IV), and (VI) are shown in Fig. S-2 in the ESM. Table 1 lists the atomic ratios of Ni and Pt and the Pt loadings in the films (I)–(VI) as determined by inductively coupled plasma–atomic emission spectroscopy (ICP-AES). It can be seen that the Pt loading ranges from 0 to 7.61 μg/cm² and the atomic ratios of Ni and Pt in the films (I)–(VI) increase from

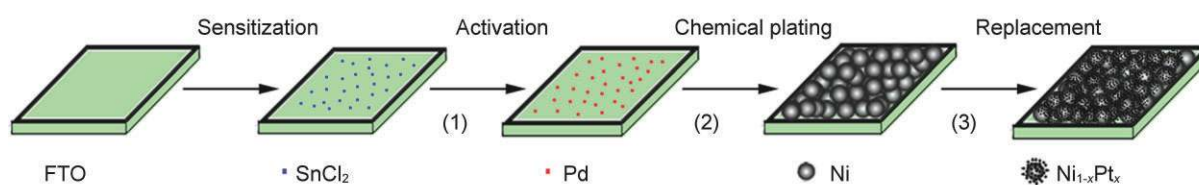**Figure 1** Schematic flow diagram for the preparation of $Ni_{1-x}Pt_x$ films

0 to 0.08 as the time of the displacement reaction was extended from 0 to 60 s. The chemical reactions involved in the preparation process can be briefly expressed as Eqs. (1)–(3):
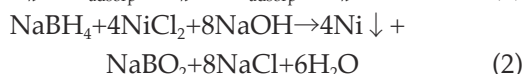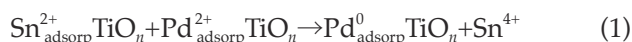
$$Sn^{2+}_{adsorp}TiO_n + Pd^{2+}_{adsorp}TiO_n \rightarrow Pd^{0}_{adsorp}TiO_n + Sn^{4+} \qquad (1)$$

$$NaBH_4 + 4NiCl_2 + 8NaOH \rightarrow 4Ni\downarrow +$$
$$NaBO_2 + 8NaCl + 6H_2O \qquad (2)$$

$$(1+x)Ni + xH_2PtCl_6 \rightarrow Ni_{1-x}Pt_x + 2xNiCl_2 + 2xHCl \qquad (3)$$

Table 1   Pt loadings in the $Ni_{1-x}Pt_x$ films obtained after different reaction times

Sample	Pt loading ($\mu g/cm^2$)	x	Reaction time (s)
I	0	0	0
II	1.32	0.02	15
III	3.41	0.04	30
IV	5.13	0.06	45
V	7.61	0.08	60
VI	6.32	1	–

1.2   Electrode characterization and electrochemical measurements

The morphologies and microstructures of the $Ni_{1-x}Pt_x$ samples were characterized by scanning electron microscopy (SEM, JEOL JSM-6700F Field Emission). The composition of the samples was studied by energy-dispersive X-ray spectroscopy (EDS) on an Oxford Link ISIS energy dispersive spectrometer attached to the SEM. The determination of the Pt loading and the Pt valance state on the FTO conductive glass was performed by ICP–AES (Thermo Jarrell Ash Corp.) and X-ray photoelectron spectroscopy (XPS, Kratos Axis Ultra DLD electron spectrometer), respectively. The as-prepared samples on the FTO conductive glass were characterized by powder X-ray diffraction (XRD, Rigaku D/max 2500 X-ray generator, Cu Kα radiation, $\lambda = 1.5405$ Å) at a scanning rate of $4(°)/$min from 20° to 80° for 2θ. The UV-visible diffuse reflectance spectra of the $Ni_{1-x}Pt_x$ coated glass samples were recorded at room temperature on a Jasco V-550 UV–vis spectrophotometer.

Electrochemical impedance spectroscopy (EIS) of the films was investigated with a PARSTAT 2273 electrochemical analyzer to determine the catalytic effect of the Pt loading in the $Ni_{1-x}Pt_x$ films [17]. For EIS testing, two symmetric electrodes were firmly clipped together with I^-/I_3^- electrolyte filling the inter-electrode space. EIS spectra were obtained at zero bias potential and 10 mV amplitude over the frequency range $0.01–10^5$ Hz [7]. Cyclic voltammetry (CV) measurements were carried out in a N_2-purged acetonitrile solution at a scan rate of 100 mV/s. The prepared $Ni_{1-x}Pt_x$ film on the FTO glass substrate, a Pt coil and a Ag/Ag$^+$ electrode were used as the photocathode, the working electrode, and the reference electrode, respectively. The electrolyte was acetonitrile containing 0.1 mol/L LiClO$_4$ as the supporting electrolyte and 10 mmol/L LiI +1 mmol/L I$_2$ as the redox couple.

The photocurrent density–voltage ($J–V$) characteristics of the solar cells based on the $Ni_{1-x}Pt_x$ films with different Pt loadings were determined using a Keithley 2400 Digital SourceMeter controlled by a computer. The porous TiO$_2$ films were prepared by a screen printing method [18, 19]. The composition of the electrolyte was 0.6 mol/L of 1,2-dimethyl-3-propylimidazolium iodide (DMPII), 0.1 mol/L of LiI, 0.05 mol/L of I$_2$, and 0.5 mol/L of t-butylpyridine (tBP) in a mixture of acetonitrile/methoxypropionitrile (volume ratio, 1:1). A 500 W xenon lamp served as the light source in combination with a band-pass filter (400–800 nm) to remove ultraviolet and infrared radiation to give a power of 100 mW/cm^2 on the surface of the test cell. Further calibration was carried out using a USB4000 plug-and-play miniature fiber optic spectrometer (Ocean Optics) to give standard AM 1.5 simulated sunlight. The active electrode area of all the DSCs was 0.16 cm^2.

2. Results and discussion

The SEM micrograph in Fig. 2(a) shows the surface morphology of the chemically plated Ni film (I). It can be seen that the film consists of homogeneously distributed spherical Ni particles, which have an average size of about 100 nm and are arranged compactly on the FTO conductive glass. As seen in Fig. 2(b), the cross section of the film is composed of three parts, I1, I2, and I3, which correspond to bare glass, the FTO conductive layer, and the Ni film layer with thickness of about 300 nm. Although
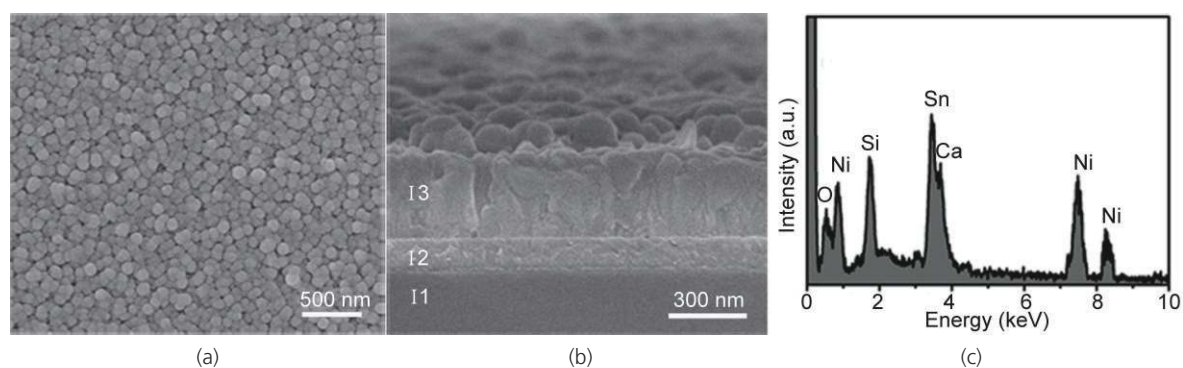
Figure 2 SEM images of the surface (a) and cross section (b) of the Ni film (Ⅰ), and the EDS spectrum (c) of the film

$NaBH_4$ was used as the reducing agent to prepare the film, no elemental boron was detected by EDS measurements (Fig. 2(c)), and thus we can assume that the film consists of pure Ni. Elements including Ca, Si, Sn, and O in the EDS spectrum originate from the FTO conductive glass.

Figure 3(a) shows the XRD pattern of the $Ni_{0.94}Pt_{0.06}$ film (Ⅳ) together with those of the pure FTO glass substrate, Pt, and Ni for comparison. Similar patterns were observed for the other $Ni_{1-x}Pt_x$ films (Ⅰ), (Ⅱ), (Ⅲ), and (Ⅴ) and the Pt film obtained by thermal decomposition (Ⅵ) (see Fig. S-3 in the ESM). The diffraction peaks of the $Ni_{0.94}Pt_{0.06}$ film (Ⅳ) can be attributed to the FTO conductive glass, except for the peaks centered at about $2\theta = 40.5°$ and 46.8°, which are slightly shifted towards higher values in comparison with the standard diffraction peaks of fcc Pt (JCPDS. No. 04-0802). This change is probably due to the incorporation of Pt atoms into the Ni crystal lattice and the partial substitution of Ni

atoms to form a $Ni_{0.94}Pt_{0.06}$ alloy, which also leads to increased conductivity of the electrode and enhanced adherence of Pt crystallites to the Ni layer [20].

Figure 3(b) shows the XPS spectrum of the $Ni_{0.94}Pt_{0.06}$ film (Ⅳ). No chloride, sodium, or potassium were found, and the O 1s and C 1s peaks can be attributed to the adsorption of oxygen and carbon on the surface of the film due to exposure to the air. The inset shows the Pt 4f region of the XPS spectrum of the $Ni_{0.94}Pt_{0.06}$ film (Ⅳ). Peaks for Pt $4f_{7/2}$ and Pt $4f_{5/2}$ centered at 71.2 eV and 74.4 eV correspond to the binding energy of Pt^0 [21]. No signals corresponding to $Pt^{Ⅱ}$ or $Pt^{Ⅳ}$ on the surface of the $Ni_{1-x}Pt_x$ films were observed by XPS. Since it is known that Pt^0 shows higher catalytic activity for the reduction of I^{3-} than $Pt^{Ⅱ}$ and $Pt^{Ⅳ}$, the XPS results suggest that the $Ni_{1-x}Pt_x$ films are appropriate photocathodes for DSCs.

The morphologies and composition of the $Ni_{1-x}Pt_x$ films were investigated by SEM, ICP, and EDS. SEM (Fig. 4(a)) shows that the surface of the $Ni_{0.94}Pt_{0.06}$

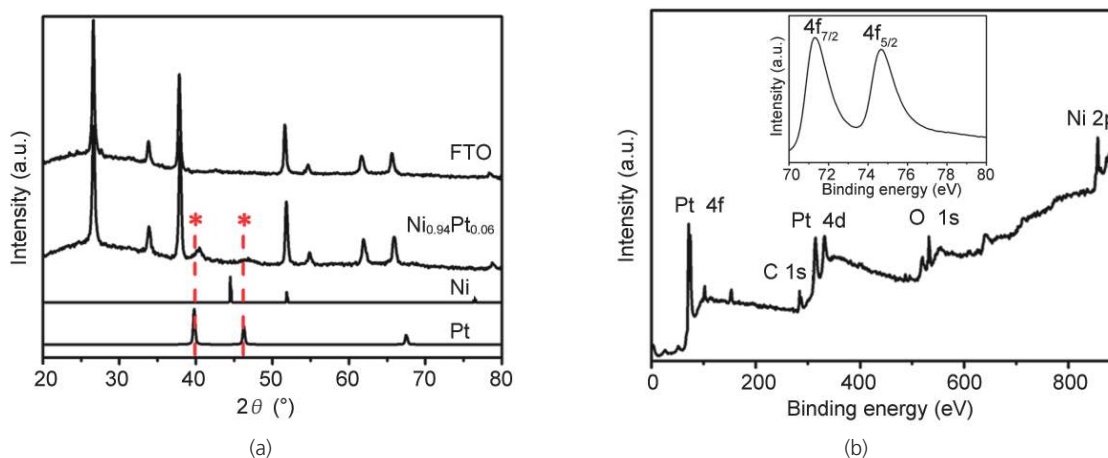**Figure 3** XRD patterns (a) and XPS spectra (b) of the as-prepared $Ni_{0.94}Pt_{0.06}$ film (Ⅳ). The inset shows the Pt 4f XPS spectrum

film (IV) consists of 100-nm spheres with a core-shell structure, as is clearly demonstrated by the higher magnification image in Fig. 4(b). The film is about 300 nm in thickness (Fig. 4(c)) and contains Pt and Ni elements, as evidenal by EDS (Fig. 4(d)). As the standard reduction potential of the $PtCl_6^{4-}$/Pt couple (0.735 V versus a normal hydrogen electrode (NHE)) is higher than that of the Ni^{2+}/Ni couple (–0.25 V vs NHE), it can be inferred that partial substitution of Ni atoms from the outer parts of the Ni sphere by Pt is thermodynamically favorable, leading to the formation of NiPt alloy nanoparticles in the shell, which are about 4–6 nm in size. The morphologies of the $Ni_{1-x}Pt_x$ (x = 0.02, 0.04, and 0.08) films (II), (III, and (V) and the Pt film obtained by thermal decomposition (VI) are shown in Figs. 4(e)–(h). The Pt loading and the size of the alloy nanoparticles increase with increasing reaction time. The initial spherical Ni structures disappear in the $Ni_{0.92}Pt_{0.08}$ film (V) (Fig. 4(g)) and nanoparticles with sizes of about 15–20 nm are formed on the surface, showing the aggregation and growth of the NiPt alloy nanoparticles during the reaction process. The Pt nanoparticles in the film obtained by conventional thermal decomposition (VI) appear as irregular

agglomerations and possess larger sizes of 25–30 nm, as displayed in Fig. 4(h). The EDS technique provides information about the metal loading and also allows mapping of the element distribution in the films. The element maps shown in the insets clearly indicate that the Pt loading increases with increasing reaction time, and the distribution of the Pt nanoparticles is homogeneous in the films, which should favor good catalytic performance as photocathodes. The SEM images, EDS spectra, and Pt 4f XPS spectra illustrated in Fig. S-4 (in the ESM) show that the properties of the $Ni_{1-x}Pt_x$ films (II), (III), and (V) and the Pt film (VI) are all very similar to those of the $Ni_{1-x}Pt_x$ film (IV).

EIS is extensively employed to investigate the kinetic performance of electrodes [22, 23]. The charge-transfer resistance, R_{ct}, appearing as a semicircle at the high-frequency end of the EIS spectra, represents electron transfer to and from the triiodide. The smaller the semicircle is, the better the catalytic performance is. Figure 5 shows the electrical impedance spectra for the cells with $Ni_{1-x}Pt_x$ films (I)–(V) and Pt film (VI), while Table 2 summarizes the R_{ct} data for these cells. The R_{ct} value of the Ni film (I) is about 1000 $\Omega \cdot cm^2$, indicating it has little catalytic effect on the triiodide reduction.
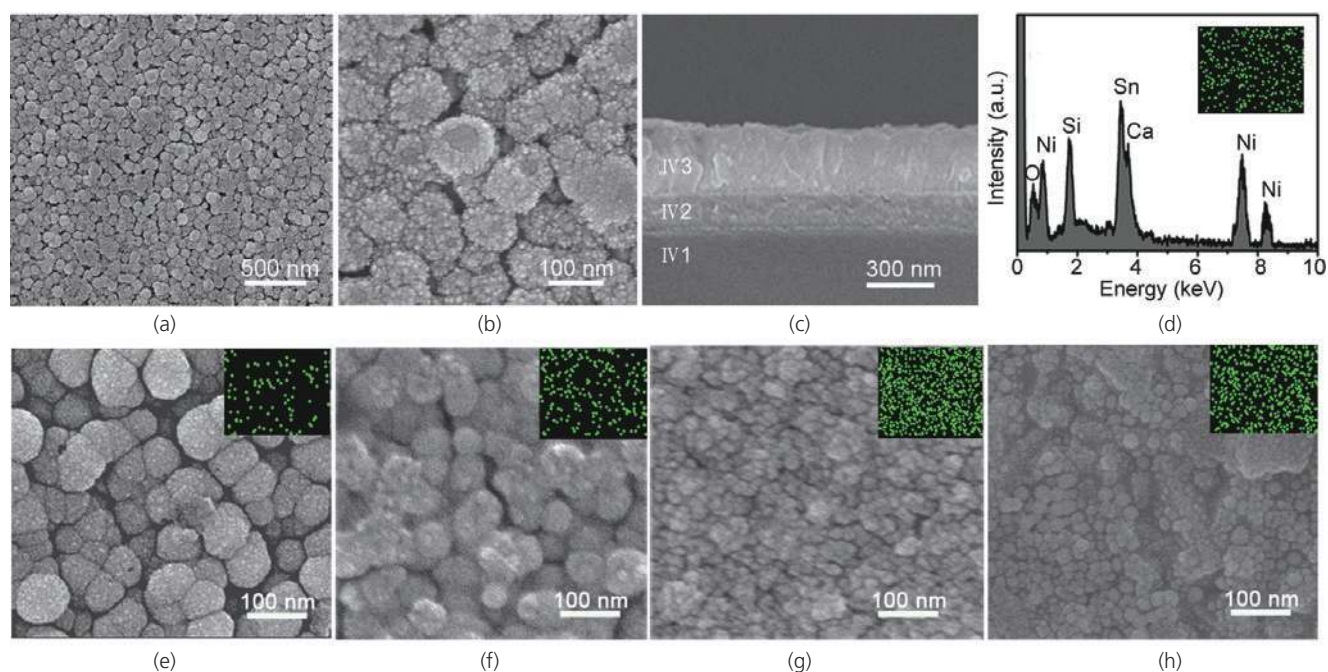

Figure 4 SEM images of the surface (a), (b) and the cross section (c) of the $Ni_{0.94}Pt_{0.06}$ film (IV), and the EDS spectrum of the film (d). SEM images of films of $Ni_{0.98}Pt_{0.02}$ (II) (e), $Ni_{0.96}Pt_{0.04}$ (III) (f), $Ni_{0.92}Pt_{0.08}$ (V) (g), and pure Pt (VI) (h). The insets show the elemental distribution maps for Pt

The R_{ct} values of the $Ni_{1-x}Pt_x$ films decrease from 19 $\Omega \cdot cm^2$ in film (II) to 0.51 $\Omega \cdot cm^2$ in film (IV). Furthermore, the sheet resistances of the $Ni_{1-x}Pt_x$ films are smaller than that of the Pt film (VI), which is ascribed to the stronger adhesion of films to the FTO substrate. It is known that the optimum kinetic catalytic performance generally depends on the interrelation between the Pt loading and the size of the catalyst particles [24]. With the extension of the reaction time, the Pt loading in the films is increased and some small compact NiPt alloy nanoparticles form on the Ni films. As a result, the electron transfer at the photocathode is accelerated and the catalytic activity is improved [6, 9]. However, no significant improvement in the charge-transfer resistance at the interface of the photocathode and the electrolyte was observed when the Pt loading in the film was further increased to give the $Ni_{0.92}Pt_{0.08}$ film (V), i.e., an increase in Pt loading does not contribute to the catalytic activity of the triiodide reduction once the Pt loading achieves a certain level.
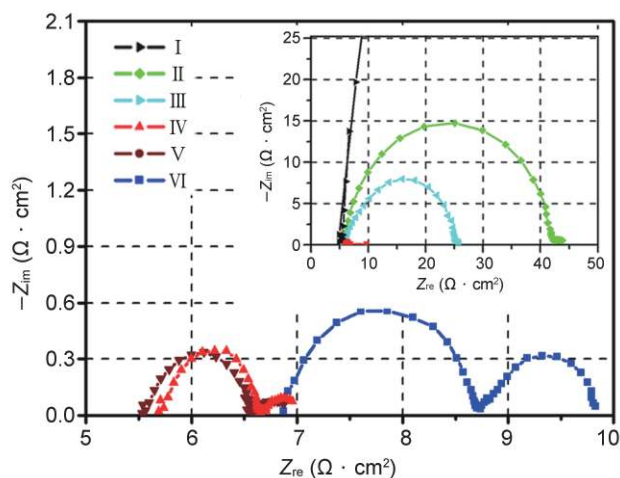

Figure 5 Electrical impedance spectra for the $Ni_{1-x}Pt_x$ films (I)–(VI). The inset shows spectra for an expanded range

**Table 2** Values of charge-transfer resistance, R_{ct}, of $Ni_{1-x}Pt_x$ films (I–VI)

Sample	I	II	III	IV	V	VI
R_{ct} ($\Omega \cdot cm^2$)	1000	19	10	0.51	0.50	0.94

To analyze the catalytic performance of the films (I)–(VI), cyclic voltammograms were performed using a three-electrode system in acetonitrile solution containing $LiClO_4$ as the supporting electrolyte and $LiI + I^2$ as the redox couple. The scanned potential ranged from 1.0 V to –0.8 V versus a saturated Ag/AgCl reference electrode. As shown in Fig. 6, the Ni film exhibited poor catalytic behavior for the redox reactions of the I^-/I_3^- couple with weak oxidation/reduction peaks. Two well-defined reduction peaks and the corresponding oxidation peaks were visible when the $Ni_{1-x}Pt_x$ films (II)–(V) and the Pt film (VI) were used as the working electrodes. The absolute values of cathodic peak currents were almost the same as those of the corresponding anodic peak currents. In an anodic sweep, iodide is oxidized to triiodide (anodic peak 1) and then to iodine (anodic peak 2) according to reactions (4) and (5), respectively.

$$\text{Anodic peak 1: } 3I^- \rightarrow I_3^- + 2e^- \qquad (4)$$
$$\text{Anodic peak 2: } 2I_3^- \rightarrow 3I_2 + 2e^- \qquad (5)$$
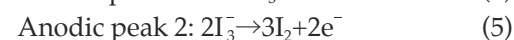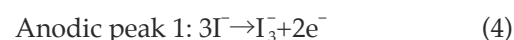
Conversely, iodine is first reduced to triiodide (cathodic peak 1′) and then to iodide (cathodic peak 2′) when the potential scan is reversed [25]. These two reduction reactions can be expressed by Eqs. (6) and (7).

$$\text{Cathodic peak 1′: } 3I_2 + 2e^- \rightarrow 2I_3^- \qquad (6)$$
$$\text{Cathodic peak 2′: } I_3^- + 2e^- \rightarrow 3I_3^- \qquad (7)$$
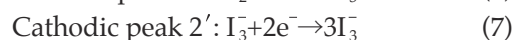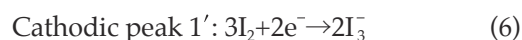
The oxidation and reduction peaks of I^-/I_3^- for the different $Ni_{1-x}Pt_x$ films were all quite similar and the largest current density was observed when the $Ni_{0.94}Pt_{0.06}$ film (IV) was used as the working electrode; this can be attributed to the presence of small alloy nanoparticles, the porous structure of the film, and the appropriate Pt loading [24]. The high current density of the films is advantageous for application in DSCs.
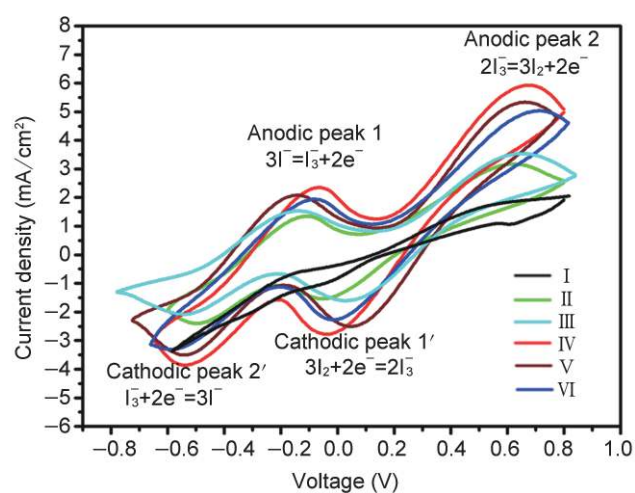

Figure 6 Cyclic voltammograms of the $Ni_{1-x}Pt_x$ films (I)–(VI)

It is well known that the light reflection and light absorption ability of the electrodes affect the light-harvesting efficiency of DSCs [14, 26]. Figure 7 shows the UV-vis reflection spectra of the $Ni_{1-x}Pt_x$ films (I)–(VI). It can be seen that the reflection intensity is very poor, between 10% and 15% for the FTO glass itself and the Pt film (VI). In contrast, the reflection intensities of the $Ni_{1-x}Pt_x$ films (I)–(V) are much higher and show a similar increase from ~30% at a wavelength of 200 nm to ~75% at 850 nm. The increased light reflectance is advantageous, as it reduces losses of the light and enhances the absorption of the light. Therefore, the $Ni_{1-x}Pt_x$ photocathodes can help to improve the light harvesting efficiency and increase the conversion efficiency of DSCs.
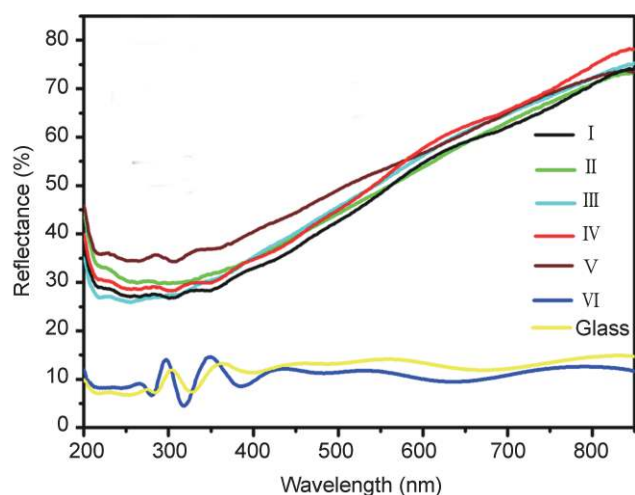

Figure 7 UV-vis spectra of the FTO conductive glass and $Ni_{1-x}Pt_x$ films (I)–(VI)

Figure 8 shows the current density–voltage curves of DSCs based on the thin films (I)–(VI) as the photocathode, and Table 3 summarizes the performance of the DSCs. As the Pt loading increases from film (II) to film (IV), the conversion efficiency η improves significantly, and the highest efficiency of the solar cell—with the $Ni_{0.94}Pt_{0.06}$ photocathode (IV)— is higher than that of the DSC with the Pt film electrode obtained by thermal decomposition (VI). When the photocathode is the pure Ni film (I) without Pt, the conversion efficiency η is very low, confirming that the catalytic effect originates mainly from Pt [6]. As seen from Table 3, the voltages of the cells V_{oc}

assembled with different $Ni_{1-x}Pt_x$ films display only slight differences. Hence, the key factors affecting the conversion efficiency are the fill factor, FF, and the short-circuit current density, J_{sc}. The fill factor of the photocurrent–voltage curve is determined by the combined resistance of the TiO_2 porous electrode, the photocathode, and the electrolyte [22]. As the DSCs were fabricated by the same procedures and the same materials were used, the resistances of the TiO_2 porous electrode and the electrolyte can be considered to be the same. Accordingly, the high fill factors for films (II)–(VI) are mainly related to the low resistance of the photocathodes, which is associated with the small sizes and limited amounts of the cathode nanoparticles [25, 27]. The increase in the short-circuit current density of the DSCs based on films (II)–(VI) relative to that of the pure nickel film

Table 3 Performance characteristics of DSCs with the $Ni_{1-x}Pt_x$ (I)–(VI) films as the photocathode

Film No.	V_{oc} (mV)	J_{sc} (mA / cm^2)	FF (%)	η (%)
I	654	11.60	8.8	0.092
II	715	15.91	46.3	5.27
III	732	15.73	56.8	6.54
IV	736	16.79	66.4	8.21
V	740	17.01	65.0	8.18
VI	745	15.6	63.1	7.33

V_{oc} represents open-circuit photovoltage; Jsc represents short-circuit photocurrent density; FF represents fill factor; η, overall conversion efficiency, is calculated as follows, $\eta = V_{oc}J_{sc}FF/P_{in}$, in which P_{in} is the intensity of the incident light.
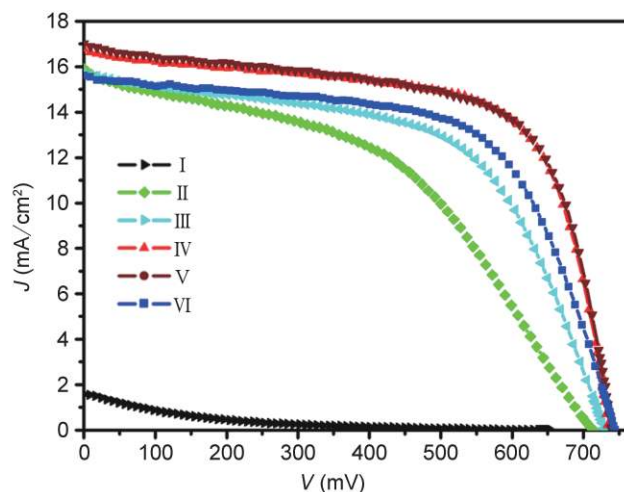

Figure 8 Photocurrent density–voltage (J–V) curves for DSCs assembled with $Ni_{1-x}Pt_x$ films (I)–(VI) as the photocathode

(I) may be attributed to the small sizes of the NiPt alloy particles and the improved light harvesting efficiency owing to the superior light reflection of the $Ni_{1-x}Pt_x$ photocathodes (II)–(VI).

The stability of the sealed solar cell with the $Ni_{0.94}Pt_{0.06}$ film (IV) photocathode, which has the best overall cell performance, was investigated in the dark at room temperature [28]. The results are shown in Fig. 9. During the test, the open voltage V_{oc} increased slightly while the current density J_{sc} and fill factor FF both decreased by a small extent. The energy conversion efficiency η of the solar cell retained 95% of its initial value after 500 h. This excellent stability further indicates that the $Ni_{1-x}Pt_x$ films are suitable materials for the photocathode in DSCs.
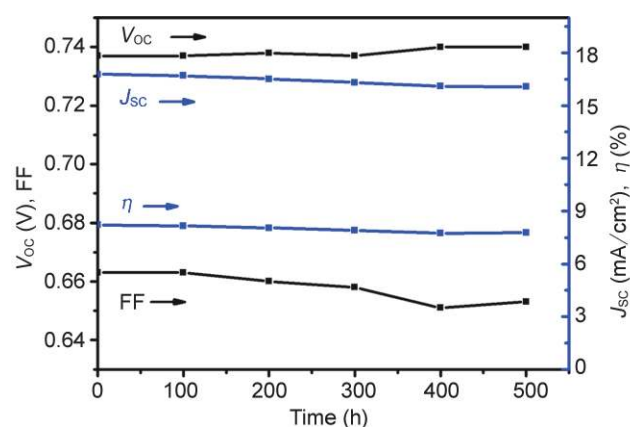

Figure 9 A short-term evaluation of the stability of the *J–V* parameters of the sealed DSC with the $Ni_{0.94}Pt_{0.06}$ film (IV) as the photocathode

3. Conclusions

We have fabricated $Ni_{1-x}Pt_x$ ($x =$ 0, 0.02, 0.04, 0.06, and 0.08) films by the displacement reaction of chemically plated Ni films on FTO conductive glass substrates with H_2PtCl_6 solution at room temperature and investigated their application as photocathodes in DSCs. By optimizing the reaction time of the Ni films, we can obtain a DSC with higher conversion efficiency than a solar cell with a pure Pt photocathode obtained by conventional thermal decomposition. The solar cell based on the $Ni_{0.94}Pt_{0.06}$ film (IV) shows excellent stability. The superior performance of the $Ni_{0.94}Pt_{0.06}$ photocathode arises from its high catalytic performance toward triiodide reduction, high light

reflectance, and low charge-transfer resistance. This study shows that the as-prepared $Ni_{0.94}Pt_{0.06}$ film IV with a low Pt loading of 5.13 μg/cm^2 is promising material for the photocathode in commercial DSCs.

References

[1] Gur, I.; Fromer, N. A.; Geier, M. L.; Alivisatos, A. P. Air-stable all-inorganic nanocrystal solar cells processed from solution. *Science* **2005**, *310*, 462–465.

[2] Liu, J. F.; Chen, W.; Liu, X. W.; Zhou, K. B.; Li, Y. D. Au/LaVO$_4$ nanocomposite: Preparation, characterization, and catalytic activity for CO oxidation. *Nano Res.* **2008**, *1*, 46–55.

[3] Qin, Y.; Wang, X. D.; Wang, Z. L. Microfibre-nanowire hybrid structure for energy scavenging. *Nature* **2008**, *451*, 801–813.

[4] Law, M.; Greene, L. E.; Johnson, J. C.; Saykally, R.; Yang, P. D. Nanowire dye-sensitized solar cells. *Nat. Mater.* **2005**, *4*, 455–459.

[5] O'Regan, B.; Grätzel, M. A low-cost, high-efficiency solar cell based on dye-sensitized colloidal TiO$_2$ films. *Nature* **1991**, *353*, 737–740.

[6] Papageorgiou, N. Counter-electrode function in nanocrystalline photoelectrochemical cell configurations. *Coord. Chem. Rev.* **2004**, *248*, 1421–1446.

[7] Cai, F. S.; Liang, J.; Tao, Z. L.; Chen, J.; Xu, R. S. Low-Pt-loading acetylene-black cathode for high-efficient dye-sensitized solar cells. *J. Power Sources* **2008**, *177*, 631–636.

[8] Fang, X. M.; Ma, T. L.; Guan, G. Q.; Akiyama, M.; Abe, E. Performances characteristics of dye-sensitized solar cells based on counter electrodes with Pt films of different thickness. *J. Photochem. Photobiol. A: Chem.* **2004**, *164*, 179–182.

Springer

[9] Kim, S. S.; Nah, Y. C.; Noh, Y. Y.; Jo, J.; Kim, D. Y. Electrodeposited Pt for cost-efficient and flexible dye-sensitized solar cells. *Electrochim. Acta* **2006**, *51*, 3814–3819.

[10] Wei, T. C.; Wan, C. C.; Wang, Y. Y. Poly(*N*-vinyl-2-pyrrolidone)-capped platinum nanoclusters on indium-tin oxide glass as counterelectrode for dye-sensitized solar cells. *Appl. Phys. Lett*. **2006**, *88*, 103122.

[11] Ikegami, M.; Miyoshi, K.; Miyasaka, T.; Teshima, K.; Wei, T. C.; Wan, C. C.; Wang, Y. Y. Platinum/titanium bilayer deposited on polymer film as efficient counter electrodes for plastic dye-sensitized solar cells. *Appl. Phys. Lett*. **2007**, *90*, 153122.

[12] Kima, S. S.; Park, K. W.; Yuma, J. H.; Sung, Y. E. Dye-sensitized solar cells with Pt-NiO and Pt-TiO$_2$ biphase counter electrodes. *J. Photochem. Photobiol. A: Chem*. **2007**, *189*, 301–306.

[13] Wang, G. Q.; Lin, R. F.; Lin, Y.; Li, X. P.; Zhou, X. W.; Xiao, X. R. A novel high-performance counter electrode for dye-sensitized solar cells. *Electrochim. Acta* **2005**, *50*, 5546–5552.

[14] Zhu, J.; Cheng, F. Y.; Tao, Z. L.; Chen, J. Electrocatalytic methanol oxidation of Pt$_{0.5}$Ru$_{0.5-x}$Sn$_x$/C(x=0–0.5). *J. Phys. Chem. C* **2008**, *112*, 6337–6345.

[15] Mallory, G. O.; Hajdu, J. B. *Electroless Plating: Fundamentals and Applications*; American Electroplaters and Surface Finishers Society: Orlando, Fl, 1990.

[16] Sun, Y. G.; Qiao, R. Facile tuning of superhydrophobic states with Ag nanoplates. *Nano Res*. **2008**, *1*, 292–302.

[17] Li, C. S.; Zhang, S. Y.; Cheng, F. Y.; Ji, W. Q.; Chen, J. Porous LiFePO$_4$/NiP composite nanospheres as the cathode materials in rechargeable lithium ion batteries. *Nano Res*. **2008**, *1*, 242–248.

[18] Shi, J. F.; Liang, J.; Peng, S. J.; Xu, W.; Pei, J.; Chen J. Synthesis, characterization and electrochemical properties of a compact titanium dioxide layer. *Solid State Sci*. **2009**, *11*, 433–438.

[19] Liang, M.; Xu, W.; Cai, F. S.; Chen, P. Q.; Peng, B.; Chen, J.; Li, Z. M. New triphenylamine-based organic dyes for efficient dye-sensitized solar cells. *J. Phys. Chem. C* **2007**, *111*, 4465–4472.

[20] Cheng, F. Y.; Ma, H.; Li, Y. M.; Chen, J. Ni$_{1-x}$Pt$_x$ (x=0–0.12) hollow spheres as catalysts for hydrogen generation from ammonia borane. *Inorg. Chem*. **2007**, *46*, 788–794.

[21] Chen, J. Y.; Herricks, T.; Geissler, M.; Xia, Y. N. Single-crystal nanowires of platinum can be synthesized by controlling the reaction rate of a polyol process. *J. Am. Chem. Soc*. **2004**, *126*, 10854–10855.

[22] Wang, Q.; Ito, S.; Grätzel, M.; Fabregat-Santiago, F.; Mora-Seró, I.; Bisquert, J.; Bessho, T.; Imai, H. Characteristics of high efficiency dye-sensitized solar cells. *J. Phys. Chem. B* **2006**, *110*, 25210–25221.

[23] Kuang, D. B.; Ito, S.; Wenger, B.; Klein, C.; Moser, J. E.; Humphry-Baker, R.; Zakeeruddin, S. M.; Grätzel, M. High molar extinction coefficient heteroleptic ruthenium complexes for thin film dye-sensitized solar cells. *J. Am. Chem. Soc*. **2006**, *128*, 4146–4154.

[24] Papageorgiou, N.; Maier, W. F.; Grätzel, M. An iodine/triiodide reduction electrocatalyst for aqueous and organic media. *J. Electrochem. Soc*. **1997**, *144*, 876–884.

[25] Wei, T. C.; Wan, C. C.; Wang, Y. Y.; Chen, C. M.; Shiu, H. S. Immobilization of poly(*N*-vinyl-2-pyrrolidone)-capped platinum nanoclusters on indium tin oxide glass and its application in dye-sensitized solar cells. *J. Phys. Chem. C* **2007**, *111*, 4847–4853.

[26] Liu, J. F.; Yao, Q. H.; Li Y. D. Effects of downconversion luminescent film in dye-sensitized solar cells. *Appl. Phys. Lett*. **2006**, *88*, 173119.

[27] Zhu, K.; Neale, N. R.; Miedaner, A.; Frank, A. J. Enhanced charge-collection efficiencies and light scattering in dye-sensitized solar cells using oriented TiO$_2$ nanotubes arrays. *Nano Lett*. **2007**, *7*, 69–74.

[28] Pei, J.; Peng, S. J.; Shi, J. F.; Liang, Y. L.; Tao, Z. L.; Liang, J.; Chen, J. Triphenylamine-based organic dye containing the diphenylvinyl and rhodanine-3-acetic acid moieties for efficient dye-sensitized solar cells. *J. Power Sources* **2009**, *187*, 620–626.